

Coherence of a field-gradient-driven singlet-triplet qubit coupled to many-electron spin states in $^{28}\text{Si}/\text{SiGe}$

Younguk Song^{1†}, Jonginn Yun^{1†}, Jehyun Kim¹, Wonjin Jang¹, Hyeongyu Jang¹, Jaemin Park¹, Min-Kyun Cho¹, Hanseo Sohn¹, Noritaka Usami², Satoru Miyamoto², Kohei M. Itoh³,
and Dohun Kim^{1*}

¹*Department of Physics and Astronomy, and Institute of Applied Physics, Seoul National University, Seoul 08826, Korea*

²*Graduate School of Engineering, Nagoya University, Nagoya, Japan*

³*Department of Applied Physics and Physico-Informatics, Keio University, Yokohama, Japan*

†These authors contributed equally to this work.

**Corresponding author: dohunkim@snu.ac.kr*

Engineered spin-electric coupling enables spin qubits in semiconductor nanostructures to be manipulated efficiently and addressed individually. While synthetic spin-orbit coupling using a micromagnet is widely used for driving qubits based on single spins in silicon, corresponding demonstration for encoded spin qubits is so far limited to natural silicon. Here, we demonstrate fast singlet-triplet qubit oscillation (~ 100 MHz) in a gate-defined double quantum dot in $^{28}\text{Si}/\text{SiGe}$ with an on-chip micromagnet with which we show the oscillation quality factor of an encoded spin qubit exceeding 580. The coherence time T_2^* is analyzed as a function of potential detuning and an external magnetic field. In weak magnetic fields, the coherence is limited by fast noise compared to the data acquisition time, which limits $T_2^* < 1$ μs in the ergodic limit. We present evidence of sizable and coherent coupling of the qubit with the spin states of a nearby quantum dot, demonstrating that appropriate spin-electric coupling may enable a charge-based two-qubit gate in a (1,1) charge configuration.

Balancing the manipulation speed and coherence time, which often play opposing roles, has been a major goal of semiconductor quantum dot-based quantum information processing platforms¹⁻³ to maximize the qubit control fidelity. The electrical control of spin states is a representative example where, depending on the properties of the host material, either intrinsic^{4,5} or extrinsic^{6,7} spin-electric coupling methods have been explored. While strong spin-orbit coupling in compound semiconductors such as InAs and InSb enables fast Rabi oscillations^{4,5}, uncontrolled and substantial susceptibility to charge noise limits the inhomogeneous coherence time T_2^* to the order of tens of nanoseconds. More recently, hole spins in group IV materials such as Ge [8] and Si [9] or electron spins in the Si-MOS structure¹⁰ have been attracting much attention due to a more favorable ratio between the spin-orbit-based control speed and coherence time.

The electrons in silicon, in particular in the Si/SiGe heterostructure, have small intrinsic spin-orbit coupling¹¹; therefore, an extrinsic method such as a micromagnet is necessary to rapidly manipulate its spin states. For single-spin qubits, the placement of an on-chip micromagnet has proven effective for both natural^{7,12} and isotopically enriched silicon¹³ in Si/SiGe and Si-MOS structures, where the field gradient provides fast control while not severely compromising the spin coherence. In the case of the silicon-based two-electron singlet-triplet qubit, however, the efficiency of the technique involving a micromagnet has not been fully examined. Previous studies of singlet-triplet qubit operation either used a small field gradient¹⁴ or relied on the modulation of the exchange energy¹⁵ in natural silicon. Exploration of the micromagnet technique with a field gradient in the intermediate range in isotopically purified silicon would thus be important for optimizing spin-electric coupling. In addition, this approach would enable this route to be compared with other methods such as the recently demonstrated spin-valley-driven coherent singlet-triplet oscillation in silicon^{16,17}.

Here, we demonstrate singlet-triplet qubit oscillation in a gate-defined double quantum dot in $^{28}\text{Si}/\text{SiGe}$. An on-chip micromagnet is used to generate a magnetic field gradient that is sufficient to allow fast manipulation (oscillation frequency $f_Q \sim 100$ MHz), while benefiting from high spin coherence by isotopic enrichment. We measure the variation in the spin-electric coupling strength in the large valley-splitting regime (> 175 μeV) in which an appropriate field gradient enables an encoded spin qubit to attain an oscillation quality factor over 580. We also present the analysis of the variation in T_2^* as a function of experimental parameters such as detuning ε , magnetic field $B_{z,\text{ext}}$, and gate tuning conditions, exploring the origin of the dominant noise source in the system. Moreover, we present evidence that the qubit engages in sizable and coherent coupling with the spin states of a nearby quantum dot, thereby demonstrating that the appropriate amount of spin-electric coupling may enable a novel type of two-qubit gates of encoded spin qubits.

The triple quantum dot system

Figure 1a shows a multiple quantum dot device fabricated on top of a $^{28}\text{Si}/\text{SiGe}$ heterostructure (see Methods for details of the material structure and device fabrication). We focus on a two-electron singlet-triplet (ST_0) qubit formed by the gate electrodes near the left Ohmic contact and a global top gate (not shown) while the regions beneath the other electrodes are fully accumulated. The general Hamiltonian H of the ST_0 qubit can be expressed as $H = J(\varepsilon)\sigma_z + \Delta B_z \sigma_x$, where $J(\varepsilon)$ is a ε -dependent exchange interaction with the Pauli matrix $\sigma_{\Gamma=x,y,z}$. ΔB_z is the magnetic field difference between the quantum dots constituting the qubit and is denoted in the frequency unit Hz using $Tg\mu_B/h$, where g , μ_B , and h are the Lande g -factor of the electrons in silicon, the Bohr magneton, and Planck's constant, respectively.

Additionally, we formed a third, many-electron quantum dot next to the ST_0 qubit to study the capacitive interaction between them. The design of the micromagnet on top of the is similar to the ones used previously¹⁸. High frequency and synchronous voltage pulses, combined with the DC voltage through bias tees, were input to gates V_1 , V_2 , and V_T . Fast RF reflectometry^{19,20} was performed by injecting a carrier signal with a frequency of approximately 125 MHz and power of -100 dBm at the Ohmic contact of the RF single-electron transistors on the left (see Fig. 1a). The reflected power was monitored through a chain of cryogenic and room temperature amplification and subsequent homodyne detection. The device was operated in a dilution refrigerator with a base temperature of approximately ≈ 7 mK, with $B_{z,\text{ext}}$ ranging from -400 mT to 400 mT applied in the direction shown in Fig. 1a.

Figure 1b shows the charge stability diagram of the ST_0 qubit coupled with a many-electron quantum dot. The full specification of the number of electrons in the left, middle, and right quantum dots (QD_L , QD_M , QD_R , see green circles in Fig. 1a) are denoted as (n,m,l) , whereas the (n,m) notation is used whenever we focus on the ST_0 qubit only. A voltage pulse with a width of approximately 10 ns and rise time of 0.5 ns is input to V_1 and V_2 in the directions indicated by the red arrows in Fig. 1b. Near the charge transition from $(0,2,N)$ to $(1,1,N)$, the pulse abruptly changes the Hamiltonian to the form $H = \Delta B_z \sigma_x$, where the spin state initialized to the singlet rotates around the x -axis on the Bloch sphere (Larmor oscillations¹¹), thereby resulting in a non-zero triplet state probability P_T . The discrimination of the resultant excited state population is conventionally performed by Pauli spin-blockade (PSB)-based spin-to-charge conversion^{2,11,21} where the singlet and triplet spin states are mapped to the $(0,2)$ and $(1,1)$ charge configurations, respectively. However, ΔB_z produced by the micromagnet facilitates relaxation of the transient triplet $(1,1)$ to the singlet $(0,2)$ by mixing with the singlet $(1,1)$ state, which makes a high-fidelity single-shot readout problematic²².

To circumvent the problem, we adopted one of the latched-PSB techniques that maps the triplet state to a long-lived metastable charge configuration^{23–25}. Pioneered in a similar experiment performed in a GaAs triplet quantum dot system²⁴, the version we used converts the triplet state (1,1) to the (1,2) state by rapidly loading an electron from the reservoir at a tunneling rate greater than the sensor bandwidth of 10 MHz (Fig. 1c, middle panel, see also inset in Fig. 1b). On the other hand, tunneling to the reservoir on the left is tuned to be of the order of 10 Hz. At this rate, the metastable (1,2) state can relax to a singlet (0,2) state only by indirect and slow tunneling of an electron from QD_L to the reservoir on the right (Fig. 1c, rightmost panel). Along with the higher signal contrast of a charge of one electron compared with conventional PSB, the prolonged relaxation time of the triplet states enables fast and high-fidelity single-shot measurement. The fast measurement capability is also important to examine the extent to which the variation in the qubit coherence time depends on the total data acquisition time to determine the effect of slow charge noise^{26–28}, as discussed in detail below.

Figure 1d shows the magnetospectroscopy measurements of the valley splitting²⁹ for QD_L and QD_M. By observing the crossover of the ground state from the singlet to the triplet by measuring the dependence of the energy required to add the second electron to each dot on $B_{z,\text{ext}}$, we obtain the valley splitting $\sim 175 \mu\text{eV}$ ($257 \mu\text{eV}$) in QD_L (QD_M). The result confirms that the valley splitting in our device is at the largest energy scale of at least twice that of the Zeeman splitting at the maximum $B_{z,\text{ext}}$ applied in this study. Thus, we ignore the valley degree of freedom in this work and focus only on the ΔB_z -driven ST₀ qubit dynamics.

Qubit dynamics driven by the field gradient

With the calibrated $\pi/2$ pulse obtained from the Larmor oscillation measurement at the pulse amplitude $|V_1| = |V_2| = 270$ mV, we construct a three-step pulse sequence for Ramsey interferometry (Fig. 2a). During the second step, at the pulse amplitude of free evolution V_{evol} , the qubit evolves around the axis of the Bloch sphere determined by the ratio of $J(V_{\text{evol}})$ and ΔB_z . Figure 2b shows a representative quantum oscillation at $V_{\text{evol}} = 770$ mV under the representative tuning conditions. This demonstrates a record-high^{11,14,15} oscillation quality factor $Q^* = f_Q \times T_2^* = 116.25$ MHz \times 4.8 μ s = 558 of a ΔB_z -driven ST₀ qubit rotation in the deep (1,1) charge configuration. In addition, high-resolution measurement (10,000 shots per data point with a single-shot readout time of 20 μ s) of the first few oscillations (Fig. 2b, left panel) shows a readout visibility of $\sim 85\%$ (see Supplementary Information S1 for details on the signal-to-noise ratio).

To more fully understand spin-electric coupling and its effect on the coherence time, we mapped the dependence on the free evolution time t_{evol} and V_{evol} of the Ramsey interference at $B_{z,\text{ext}} = 300$ mT, as shown in Fig. 2c. The oscillation observed for $V_{\text{evol}} < 0.1$ V shows the fast but short-lived oscillation driven by J (marked as \bullet in Fig. 2d and the corresponding schematic diagram in Fig. 2e), whereas the oscillations driven by ΔB_z exhibit prolonged T_2^* (white dashed contour in Fig. 2c) for $V_{\text{evol}} > 0.1$ V due to the lower charge noise susceptibility df_Q/dV_{evol} . In this regime, the data in the time and frequency domains exhibit the following main features. First, f_Q is generally linearly dependent on V_{evol} , which arises from the presence of the micromagnet (see \blacksquare and \blackstar in Fig. 2d), and this is consistent with the previously observed linear shift of the single-spin resonance frequency in silicon in the presence of the synthetic field gradient¹³. Second, T_2^* depends non-monotonically on V_{evol} . In particular, a significant decrease in T_2^* is observed in the vicinity of $V_{\text{evol}} = 0.35$ V (near \blacklozenge in Fig. 2d). Third, f_Q undergoes an abrupt frequency shift of about $\Delta f_Q \sim 1.7$ MHz at approximately $V_{\text{evol}} = 0.45$ V

(▲ in Fig. 2d). Estimated from the calibrated lever arm of 0.023, the cross-talk effect of $V_{\text{evol}} = 0.45$ V on QD_R shifts the chemical potential of QD_R to the Fermi-level of the right contact E_F where the ground state charge transition occurs. Therefore, the observed $\Delta f_Q \sim 1.7$ MHz per one electron change is the measurement of the capacitive coupling between the ST_0 qubit and QD_R . We additionally verified this interpretation by adjusting the DC tuning of the plunger gate of QD_R and by observing the systematic shifts of the point ▲ (see Supplementary Information S2).

In general, the charge fluctuation in QD_R adversely affects the coherence of the capacitively coupled qubit. However, we note that $V_{\text{evol}} = 0.35$ V (near ● in Fig. 2d) showing the lowest T_2^* occurs below $V_{\text{evol}} = 0.45$ V (▲ in Fig. 2d) where QD_R experiences the maximum charge fluctuation. Assuming that non-negligible spin-dependent coupling occurs between the ST_0 qubit and the Zeeman-split ground and excited spin states in QD_R occupied by N electrons (E_g and E_e , respectively), the qualitative interpretation of this phenomenon is as follows (See Supplementary Information S3 for data supporting spin-dependent coupling). For detuning near ■, the spin state in QD_R remains in the ground state with high fidelity as both E_g and E_e are well below E_F , and the spin-dependent charge fluctuation is low. From point ■ to ▲, as E_e approaches and passes E_F , fast tunneling between QD_R and the reservoir through E_e leads to enhanced spin-dependent charge number fluctuation. This fluctuation reduces T_2^* and produces a small frequency shift of $\Delta f_Q \sim 0.4$ MHz (red arrows in Fig. 2d). In this regime, the spin state in QD_R is expected to be a mixed state because of the non-negligible average occupation in E_e . The maximum charge fluctuation, hence the minimum T_2^* , is expected to occur when E_e approximates E_F , which corresponds to the point ●. Finally, at point ▲, E_g aligns with E_F , resulting in the change in the full electron number in QD_R and the appearance of the kink in time-averaged f_Q measurement.

More quantitatively, we compared the experimental results and those of the numerical simulation³⁰ using the following phenomenological Hamiltonian and Lindblad operators.

$$\begin{aligned}
H = & J(V_{\text{evol}})\sigma_z \otimes \mathbf{1} + \Delta B_z(V_{\text{evol}})\sigma_x \otimes \mathbf{1} + \beta(V_{\text{evol}})\mathbf{1} \otimes \sigma_z + \gamma(B_{z,\text{ext}})\mathbf{1} \otimes \sigma_x \\
& + J_{\text{int}}(V_{\text{evol}}) \frac{1}{e^{\eta(\beta(V_{\text{evol}}-c))} + 1} \sigma_x \otimes \sigma_z \\
L_1 = & \tau_1 \sqrt{J(V_{\text{evol}})}\sigma_z \otimes \mathbf{1}, L_2 = \tau_2 \sqrt{\beta(V_{\text{evol}})}\mathbf{1} \otimes \sigma_z
\end{aligned}$$

Here, the Hamiltonian describes the two interacting qubits, ST₀ qubit, and the two spin states of the nearby *N*-electron quantum dot, QD_R. More specifically, the Hamiltonian of the ST₀ qubit is constructed as $J(V_{\text{evol}})\sigma_z + \Delta B_z(V_{\text{evol}})\sigma_x$, where the background $\Delta B_z(V_{\text{evol}}) = 47.7 V_{\text{evol}} + 61.3$ ($0.25 \text{ V} < V_{\text{evol}} < 0.7 \text{ V}$) is estimated from Fig. 2d. We assumed that the Hamiltonian of QD_R is analogous to that of the ST₀ qubit, such that the diagonal term $\beta(V_{\text{evol}})$ is an exponential function of V_{evol} , and the off-diagonal term $\gamma(B_{z,\text{ext}})$ is a linear function of $B_{z,\text{ext}}$. Furthermore, the coupling we consider is the spin-electric coupling induced from the spatial distribution of the orbital wavefunction of QD_R depending on its spin states. In view thereof, we chose the spin-electric coupled eigenstate of QD_R as the σ_z basis and introduced the interaction between the ST₀ qubit and QD_R, which was assumed to be in the form of $\sigma_x \otimes \sigma_z$. This coupling term is multiplied by a phenomenological Fermi–Dirac distribution with proper constant *c*, η and coupling strength $J_{\text{int}}(V_{\text{evol}})$ and to incorporate the change in the charge state of the nearby *N*-electron quantum dot (see Supplementary Information S4 for details of the simulation). Additionally, the phenomenological Lindblad operators for the ST₀ qubit (L_1) and two-level system in QD_R (L_2) are introduced with the proportionality constant τ_1 (τ_2) to reflect the experimentally observed decoherence.

The inset in Fig. 2c shows the simulation result which consistently reproduces the sudden kink in the frequency near $V_{\text{evol}} = 0.45 \text{ V}$, the significant decrease in T_2^* near $V_{\text{evol}} =$

0.35 V, and the subsequent recovery of T_2^* near the kink. Overall, by comparing the result of the simulation with that of the experiment, we concluded that the kink in the frequency and the drop in T_2^* indicate capacitive coupling between the ST_0 qubit and QD_R during the charge transition of QD_R .

Coherent coupling between ST_0 qubit and many-electron spin states

We further substantiated the validity of the above analysis by showing that the experimental and simulation results were consistently comparable under different quantum dot tuning conditions. Specifically, we fine-tuned the gate voltage levels to induce significant deviations in the overall coupling strength and the decoherence rates compared with the previous tuning condition. In this new tuning, we observed the characteristic beating of the quantum oscillation below $V_{\text{evol}} < 0.42$ V, as shown in Fig. 3a. Notably, the coherence of the oscillation markedly diminished when the coupling between the two qubits became appreciable. Figure 3b enables a more detailed examination of these results and provides the line cuts that offer a clearer comparison between the oscillation traces in the uncoupled ($V_{\text{evol}} = 0.6$ V, top trace in Fig. 3b) and coupled ($V_{\text{evol}} = 0.2$ V, bottom trace in Fig. 3b) regimes.

The manifestation of the beating oscillation under this specific tuning condition suggests that two different qubit frequencies emerge depending on the spin state in QD_R , and that the interqubit coupling rate is faster than the decoherence rate, unlike the previous tuning. In addition, the beating of the oscillation suggests that, below certain V_{evol} values, the eigenstate of QD_R becomes the superposition of the states of which the orbital wavefunction directly couples with f_Q through the spin-electric coupling. The significant drop in T_2^* in the regime of sizeable coupling is again likely a consequence of the interplay between the interqubit coupling and the dephasing effect discussed in the previous section. Note that the coupling strength with

the maximum value of approximately 10 MHz also exhibits a dependence on V_{evol} , thereby highlighting the electrical tunability of the interqubit coupling strength.

This experimental result was compared with the numerical simulation, which employed the identical Hamiltonian and Lindblad operators introduced in the previous section, whose parameters were appropriately adjusted to reflect the different tuning conditions. One of the key adjustments involves the parameters of $\beta(V_{\text{evol}})$, which effectively transform the eigenstate of QD_R into the superposition of the σ_z -eigenstates for $V_{\text{evol}} < 0.4$ V, which gives rise to the observed beating of the oscillation through the spin-electric coupling $\sigma_x \otimes \sigma_z$ term. The numerical calculation consistently reproduces the experimental results, including the characteristic kink near $V_{\text{evol}} = 0.48$ V, the emergence of the beating, and the significant reduction in T_2^* throughout the coupling regime. These observations can be attributed to the mixed eigenstate of QD_R and the Lindblad operators, which effectively mimic the aforementioned dephasing effect. Overall, our spin-electric coupling scenario convincingly reproduces the experimental results for various coupling parameters.

External field dependence of ST_0 qubit coherence

We turn to discuss the dominant noise source limiting the coherence of ST_0 qubit by investigating the variation in f_Q and df_Q/dV_{evol} as a function of $B_{z,\text{ext}}$. The magnitude of the field gradient $|\Delta B_z|$ is determined by measuring f_Q of the ΔB_z -dominated Ramsey oscillations at $V_{\text{evol}} = 800$ mV for various values of $B_{z,\text{ext}}$ from 400 mT to -400 mT (Fig. 4a). Generally, $|\Delta B_z|$ was positively correlated with $B_{z,\text{ext}}$, which likely originated from the formation of multiple domains due to the demagnetization of the Co micromagnet at low $B_{z,\text{ext}}$. The calculated value expected for $|\Delta B_z|$ by simulation of the magnetic field using the Object Oriented Micromagnetic

Framework (OOMMF)^{31,32} was in qualitative agreement with the experimental observation. (see Supplementary Information S5 for details of the micromagnetic simulation).

The controllability of $|\Delta B_z|$ via $B_{z,\text{ext}}$ paved the way to test whether a decrease in $|\Delta B_z|$ could lead to a smaller df_Q/dV_{evol} and, consequently, an improved T_2^* at low $B_{z,\text{ext}}$. Figure 4b shows the dependence of df_Q/dV_{evol} on f_Q , extracted at various levels of $B_{z,\text{ext}}$ and V_{evol} . Unexpectedly, a strong correlation did not exist between f_Q and df_Q/dV_{evol} . Depending on the experimental iteration, df_Q/dV_{evol} was widely dispersed even at similar f_Q controlled by V_{evol} . We again attribute this to the nanoscale formation of multiple domains in the micromagnet, which generates a locally inhomogeneous field distribution.

Figure 4c shows T_2^* and Q^* as functions of $B_{z,\text{ext}}$ at several V_{evol} . Generally, the decreasing Q^* is predominantly the result of the rapid decrease in f_Q as the applied magnetic field $B_{z,\text{ext}}$ weakens, whereas T_2^* varies at most by a factor of two as a function of $B_{z,\text{ext}}$. The latter finding is also consistent with the observation that f_Q and df_Q/dV_{evol} are not strongly correlated. Although T_2^* tends to increase in the presence of strong $B_{z,\text{ext}}$, we argue that this is because of the interplay between the experimental data acquisition time and dominant noise band, which shifts to the low frequency at stronger $B_{z,\text{ext}}$. We confirm that extending the total data acquisition time significantly affects T_2^* at $B_{z,\text{ext}} = 400$ mT, indicating that slow charge noise compared to a given measurement time plays an important role (see Supplementary Information S6). Moreover, near $V_{\text{evol}} = 350$ mV, where T_2^* is limited by strong coupling with the spin states in QD_R and fast charge noise is therefore presumed to dominate the noise spectrum, T_2^* is nearly constant as a function of $B_{z,\text{ext}}$. In this respect, we assume that T_2^* at low $B_{z,\text{ext}}$, which approximates $1 \mu\text{s}$ regardless of the value of V_{evol} , is entirely dominated by the noise spectrum, which is faster than the measurement time. This indicates that the coherences of the ST_0 qubit are closer to the ergodic limit.

The dominance of high-frequency noise in our system is also supported by measurement of the spin-echo time T_{echo} and echoed quality factor Q_{echo} at various $B_{z,\text{ext}}$ and V_{evol} (Fig. 4d). Notably, the spin-echo enables only a minor improvement in the coherence time by a factor of at most two compared with T_2^* at low $B_{z,\text{ext}}$ of ~ 100 mT, thereby indicating that the major source of noise in this regime is in the high-frequency band. Similar ineffectiveness of the spin-echo was observed in a $^{\text{Nat}}\text{Si}/\text{SiGe}$ -based singlet-triplet qubit for non-negligible J [33]. Although a previous study³⁴ pointed out that the increased flip-flop motion of residual ^{29}Si nuclear spins at low $B_{z,\text{ext}}$ leads to the reduction of T_2^* , we rule out this possibility since this quasi-static noise would have been effectively corrected by the echo sequence. Moreover, this type of noise is more likely to occur under RF excitations needed for single-spin qubit manipulation. The absence of such control in this experiment also indicates that the mechanism of the dominant noise source at low $B_{z,\text{ext}}$ in our experiment differs from that in the previous study. The spin-echo more effectively enhances the coherence time at high $B_{z,\text{ext}} > 300$ mT, which is consistent with our scenario that, in this regime, the dominant noise primarily stems from the low-frequency band. Similar to the behavior of T_2^* , the spin-echo is not effective when the ST_0 qubit is strongly coupled with QD_R (see Fig. 4d, third panel).

We additionally compared the power spectral density (PSD) of noise for strong and weak magnetic fields, $B_{z,\text{ext}}$ (400 and 50 mT, respectively) obtained by the single-shot measurement-based rapid Bayesian estimation method^{26,35,36} (see also Supplementary Information S7) as shown in Fig. 5a. Although both of these spectra exhibit a larger white noise component compared to previous studies^{28,33}, the PSD of the spectrum at $B_{z,\text{ext}} = 50$ mT is about two orders of magnitude larger across the entire range of frequencies with different exponent α of the $1/f^\alpha$ -like power spectrum compared to the PSD at $B_{z,\text{ext}} = 400$ mT. Assuming that the frequency-independent noise extends to frequencies beyond the experimentally measured limit

of ~ 40 Hz, the result explains the overall ineffective noise refocusing via the spin-echo technique in our system, in particular at low $B_{z,\text{ext}}$. In addition, the tendency of the white noise floor to increase with decreasing $B_{z,\text{ext}}$ along with the change in α (Fig. 5b), which is generally indicative of a relative increase in the portion of fast charge noise, is consistent with the variation in T_2^* and T_{echo} , as presented in Fig. 4.

Discussion and conclusions

The origin of the rather high white noise floor in our system, which further increases at low $B_{z,\text{ext}}$, remains an open question. Although a more comprehensive understanding of the dominant noise source would require further experiments, the ineffective coherence recovery using the spin-echo technique due to relatively fast noise indicates that the noise does not predominantly originate from the increased flip-flop rate of the residual ^{29}Si nuclear spins. Based on our investigation of the signature of the nanoscale multi-domain structure as the micromagnet demagnetizes at $B_{z,\text{ext}} < 200$ mT, we speculate that the fast noise could have stemmed from the interplay between the field inhomogeneity induced by the magnetic domain structure and charge noise. This could be clarified by studying multiple devices containing micromagnets with various magnetic properties. A potential approach could involve the use of different techniques for micromagnet fabrication; for example, the deposition of magnetic material in the presence of an applied magnetic field, which is known to induce a preferential magnetization axis and hence a significantly modified hysteresis loop³⁷. This technique may enable the magnetic structure to be more stably controlled in a weak magnetic field, which would allow an investigation of the transduced noise with varying magnetic properties. Moreover, the technique could also be useful for other applications such as semiconductor-

superconductor hybrid circuits^{38,39} for long-range coupling where operation in a weak magnetic field is beneficial.

Nevertheless, we successfully demonstrated coherent ST_0 oscillations with outstanding Q^* . This was enabled by using an on-chip micromagnet technique in an isotopically purified $^{28}\text{Si}/\text{SiGe}$ heterostructure where f_Q is tunable in the (1,1) charge configuration due to the dependence of the magnetization on $B_{z,\text{ext}}$. Our findings reveal that capacitive coupling can facilitate coherent interactions between two quantum systems: the two-electron ST_0 qubit and the many-electron quantum dot. Moreover, by formulating Hamiltonians for these quantum systems and their interactions, we effectively reproduced the coherent ST_0 qubit oscillation observed in our experiments through numerical simulation. Our work also suggests areas for improvement. Even though our device was designed to allow us to coarsely tune the chemical potential of QD_R , independent control of the quantum states of QD_R was challenging because of the limited number of control lines in the current single-gate layer structure. Enhanced control over individual quantum dots and precise coupling strength modulation could be attained by adopting an overlapped gate structure⁴⁰, which may enable novel two-qubit gate schemes for encoded spin qubits in silicon.

Methods

Material structure and device fabrication

The $^{28}\text{Si}/\text{SiGe}$ heterostructure wafer was grown by a molecular beam epitaxy growth method. An isotopically purified silicon source (with a residual ^{29}Si concentration of approximately 800 ppm) was used for the strained quantum well with a thickness of 12 nm. The design of the surface gate electrode resembles that of GaAs spin qubit devices where both

quantum dot confinement and barrier gates reside in the same layer and a global accumulation gate is used for electrostatic doping. The dimensions of the accumulation gate were maintained below $2 \times 2 \mu\text{m}^2$ to minimize the parasitic capacitance²⁰, enabling proper impedance matching conditions for radio frequency (RF) reflectometry. A Co micromagnet was deposited above the accumulation gate using an e-beam evaporator, with a Au cap for the antioxidation layer.

Measurement setup

The sample was cooled to the base temperature, ~ 7 mK, with a cryogen-free dilution refrigerator (Oxford Instruments Triton-500). A sensing dot based on an RF single-electron transistor was used to detect the change in the charge state of QD_L , QD_M , and QD_R in our system. An onboard inductor of 1500 nH and a parasitic capacitance on the order of 1 pF formed an LC-tank circuit with a resonance frequency at ~ 125 MHz, which was used for RF reflectometry. Two arbitrary waveform generators (HDAWG and Operator-X+ by Zurich Instruments and Quantum Machines, respectively) were used to synchronize the multi-channel voltage pulses and timing marker generation. A high-frequency lock-in amplifier (Zurich Instruments, UHFLI) was used as a carrier generator and demodulator for homodyne detection. At room temperature, a carrier power of -40 dBm was generated which was further attenuated by -50 dB by the cryogenic attenuators and the directional coupler. The reflected signal is initially amplified by 50 dB with the cryogenic amplifier (Caltech Microwave Research Group, CITLF2 x2 in series), and then additionally amplified by 20 dB at room temperature using a custom-built RF amplifier. We used the QUA (Quantum Machines) language framework for scripting experimental sequences, performing single-shot readouts, and signal conditioning.

Data availability

The data that support the findings of this study are available from the corresponding author upon request.

Acknowledgments

This work was supported by a National Research Foundation of Korea (NRF) grant funded by the Korean Government (MSIT) (No. 2019M3E4A1080144, No. 2019M3E4A1080145, No. 2019R1A5A1027055, RS-2023-00283291, SRC Center for Quantum Coherence in Condensed Matter RS-2023-00207732, and No. 2023R1A2C2005809) and the core center program grant funded by the Ministry of Education (No. 2021R1A6C101B418). The work on the $^{28}\text{Si}/\text{SiGe}$ growth was supported by JST Moonshot R&D grant No. JPMJMS226B and JSPS Grant-in-Aid for Scientific Research (KAKENHI) grant No. JP21H01808. The authors thank Susan Coppersmith for fruitful discussions. Correspondence and requests for materials should be addressed to DK (dohunkim@snu.ac.kr).

Author contributions

DK conceived and supervised the project. YS and JK fabricated the device. YS, JY, and HJ performed the measurements and analyzed the data with WJ. JP, MC, and HS built the experimental setup and configured the measurement software. SM, NU, and KMI synthesized and provided the $^{28}\text{Si}/\text{SiGe}$ heterostructure. All the authors contributed to the preparation of the manuscript.

Competing interests

The authors declare no competing interests.

Figure captions

Figure 1.

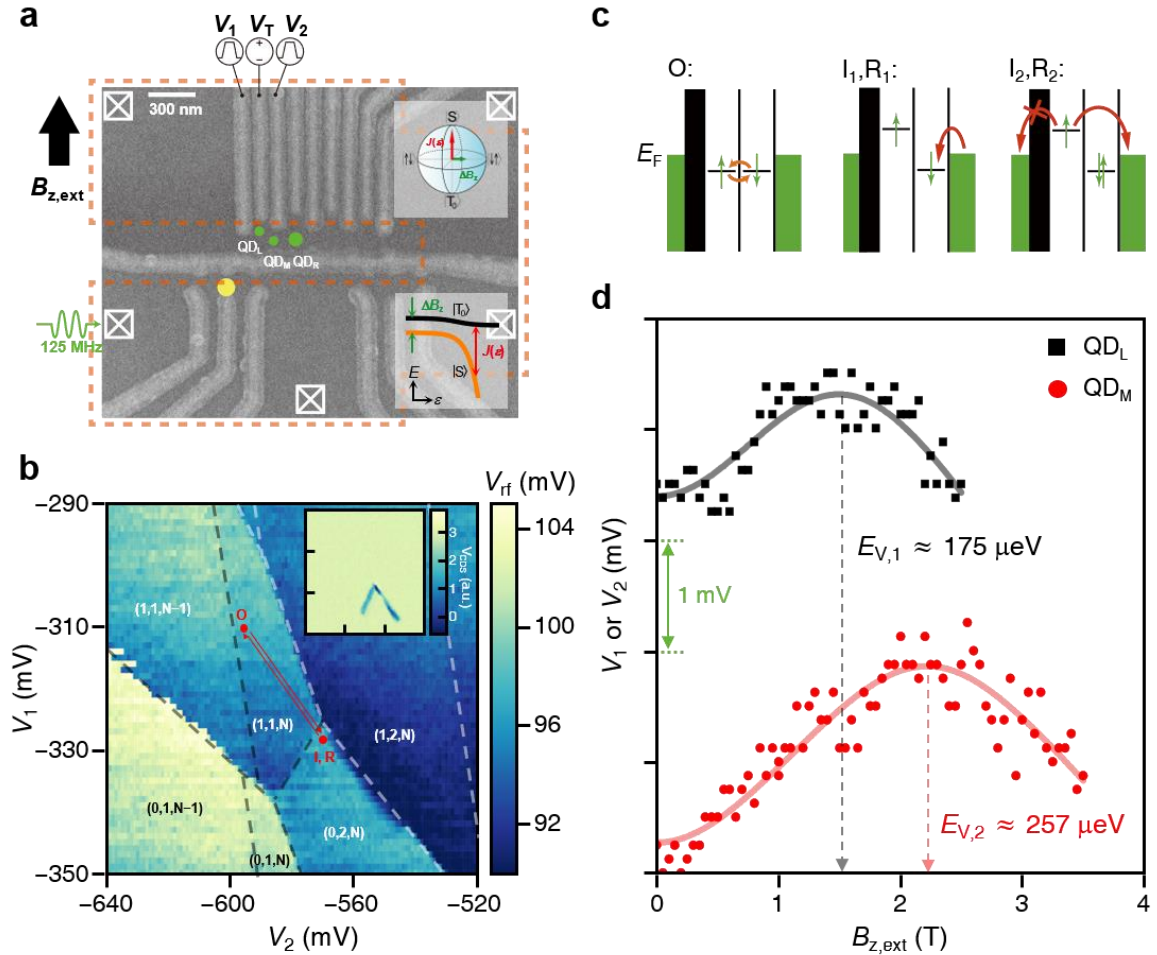


Fig. 1 | The quantum dot device and triple quantum dot system. (a) Scanning electron microscopy image of the device with the accumulation gates and Co micromagnet omitted. The black arrow indicates the direction of the external magnetic field $B_{z,ext}$. We focused on three quantum dots, indicated by the green dots labeled QD_L, QD_M, and QD_R. We used QD_L and QD_M as the ST₀ qubit and the many-electron dot QD_R to explore the coherent interactions with the ST₀ qubit. High-frequency and synchronous voltage pulses combined with DC voltage were input to gates V₁, V₂ and V_T to tune and manipulate the quantum systems. The yellow dot indicates the sensor dot based on an RF single-electron transistor, with a transpassing RF signal of ~ 125 MHz through RF Ohmic contact (indicated by the crossed squares). The orange dashed line indicates the micromagnet employed to apply a magnetic field difference ΔB_z between QD_L and QD_M. The inset in the lower right corner illustrates the general energy level of the singlet and triplet states in a two-electron ST₀ qubit, with ΔB_z and detuning the ϵ -dependent exchange interaction $J(\epsilon)$. The inset in the upper right corner depicts Bloch sphere representations of the contributions of $J(\epsilon)$ and ΔB_z concerning the qubit rotation axis, with the two-electron states of the ST₀ qubit. (b) Charge stability diagram of the primary operational region for QD_L, QD_M, and QD_R. The number in parentheses represents the number of electrons in each of the three green dots. The inset shows V_{CDS} , the correlated double sampling signal of reflected RF signal V_{rf} . We drove the ST₀ qubit to reach I-O-R sequentially by applying appropriate pulse sequences with V₁ and V₂, while additional stopover points can be added to obtain the desired final qubit state. (c) Schematic of free

evolution of the ST_0 qubit in O and the initialize/readout sequence in the I/R points in (b), respectively. (d) Measurement of the valley splitting of QD_L and QD_M via magnetospectroscopy.

Figure 2.

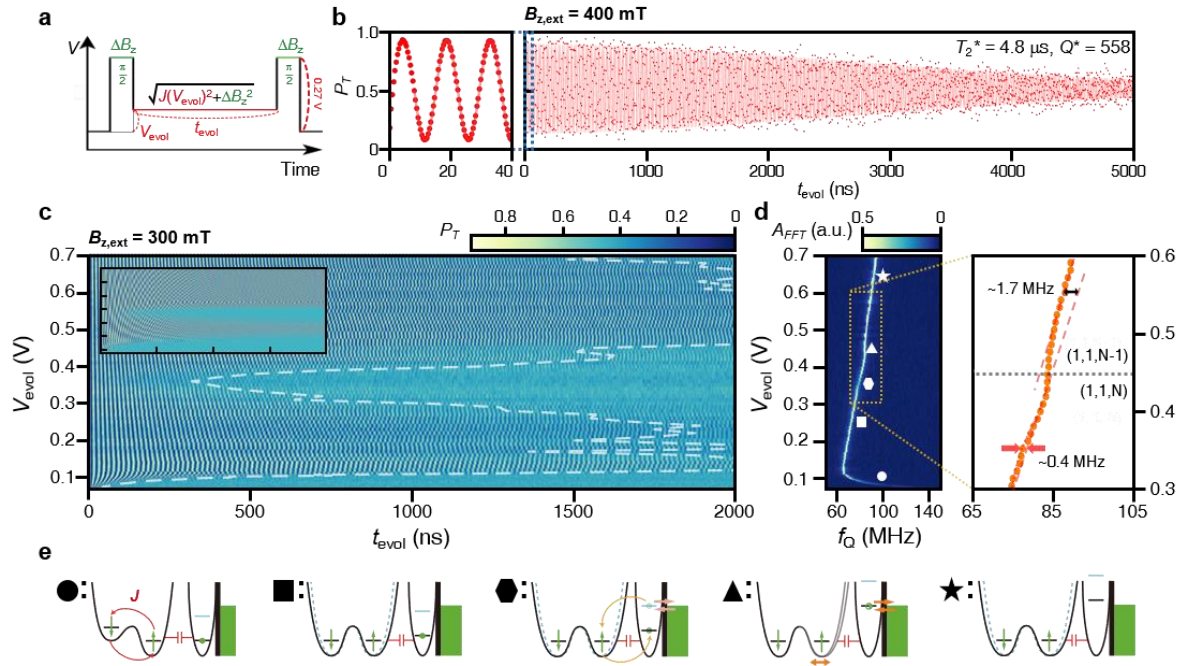


Fig. 2 | The qubit dynamics revealed by Ramsey interferometry. (a) Diagram of the pulse sequence used for Ramsey oscillation, the z-axis manipulation on the Bloch sphere with the free evolution time t_{evol} , and the pulse amplitude V_{evol} . A $\pi/2$ pulse was applied with $V_{\text{evol}} = 0.27$ V and appropriately calibrated pulse duration time. (b) Representative Ramsey oscillation with the probability of the triplet state P_T at $B_{z,\text{ext}} = 400$ mT and $V_{\text{evol}} = 770$ mV, with high coherence time T_2^* and quality factor Q^* values. The results on the left and right were averaged 10,000 and 100 times, respectively. (c) Ramsey oscillations as a function of t_{evol} and V_{evol} . The white dashed line indicates the contour line of T_2^* extracted from each Ramsey oscillation line of V_{evol} . The inset shows the numerically simulated Ramsey oscillation results. (d) Line-to-line FFT result of (c). The expected transition line of the dot on the right is indicated as a horizontal dotted line in the figure on the right. The two dashed orange lines show the linearly fitted f_Q with V_{evol} before and after the frequency shift of $\Delta f_Q \sim 1.7$ MHz during the charge transition of QD_R . A small bump with maximum $\Delta f_Q \sim 0.4$ MHz, indicated by the red arrows, is the footprint of the enhanced spin-dependent charge number fluctuation led by fast tunneling between QD_R and the electron reservoir on the right side of QD_R . (e) Schematic depicting the energy levels of each marker in (d), capacitive coupling between the ST_0 qubit and QD_R , and the tunneling between QD_R and the electron reservoir.

Figure 3.

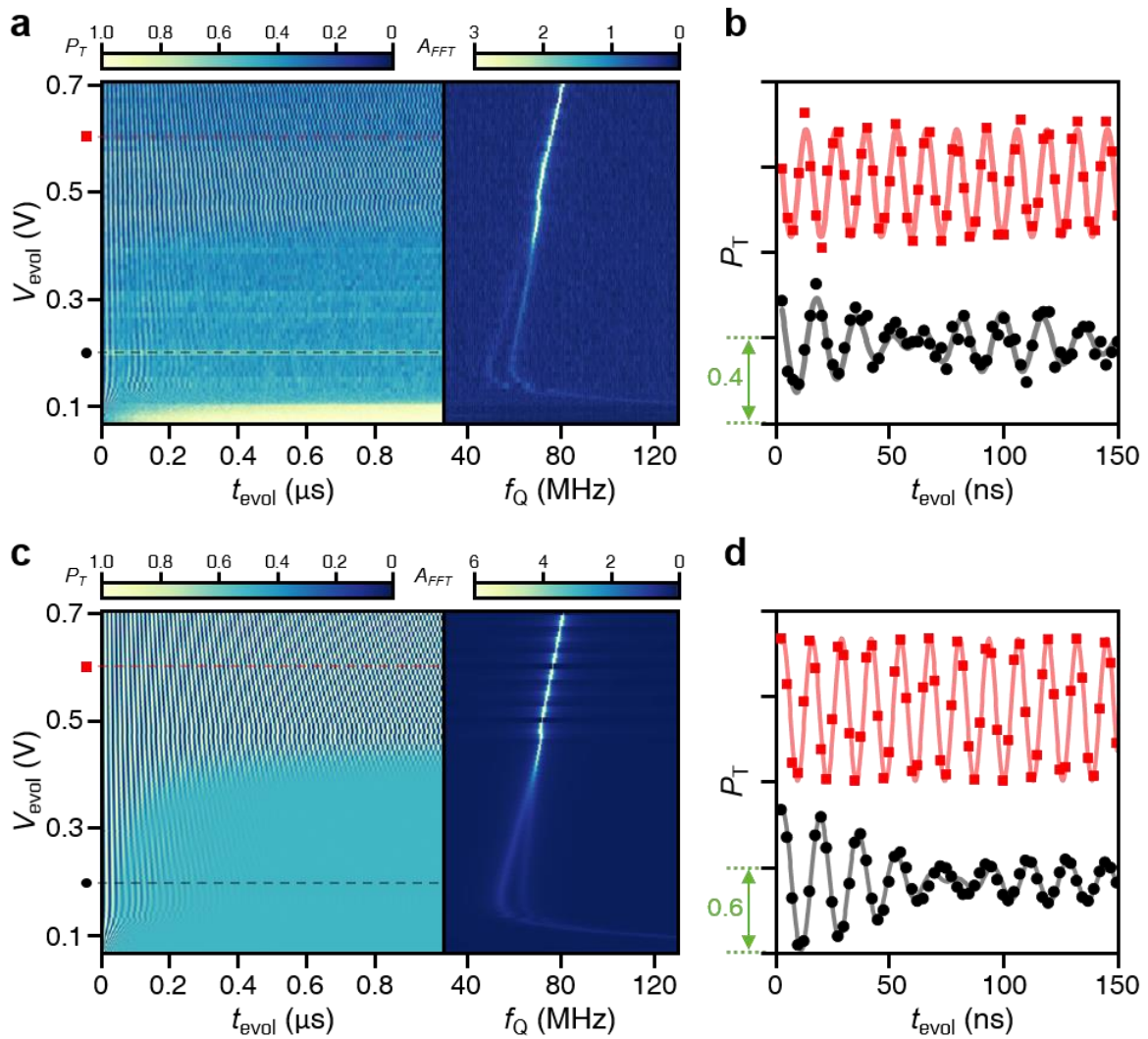


Fig. 3 | Coherent coupling between the singlet-triplet qubit and many-electron spin states. (a) Left: Ramsey oscillations as a function of t_{evol} and V_{evol} for different tuning levels. Significant dephasing appears below $V_{\text{evol}} = 0.42$ V. Right: FFT result of the figure on the left. The FFT peak exhibits the characteristic kink near $V_{\text{evol}} = 0.5$ V and linear dependence on V_{evol} in the ΔB_z -dominating regime. Characteristic splitting of the FFT peak is also manifested below $V_{\text{evol}} = 0.42$ V. (b) Ramsey oscillation trace at $V_{\text{evol}} = 0.6$ V (top, red squares) and 0.2 V (bottom, black solid circles). The beating of the oscillation at $V_{\text{evol}} = 0.2$ V is manifested. Each trace corresponds with the dashed line in the respective color in (a). The traces are offset by 1 for clarity. (c) Left: Numerical simulation of Ramsey oscillations as a function of t_{evol} and V_{evol} . The significant decoherence below $V_{\text{evol}} = 0.42$ V was reproduced consistently. Right: FFT result of the figure on the left. The FFT peak shows the kink near $V_{\text{evol}} = 0.5$ V, a V_{evol} dependence similar to the experimental results, and the characteristic splitting below $V_{\text{evol}} = 0.42$ V. (d) Simulated Ramsey oscillation trace at $V_{\text{evol}} = 0.6$ V (top, red squares) and 0.2 V (bottom, black solid circles). The simulated oscillation trace also reflects the beating of the oscillation at $V_{\text{evol}} = 0.2$ V. Each trace corresponds with the dashed line in the respective color in (c). The traces are offset by 1.2 for clarity.

Figure 4.

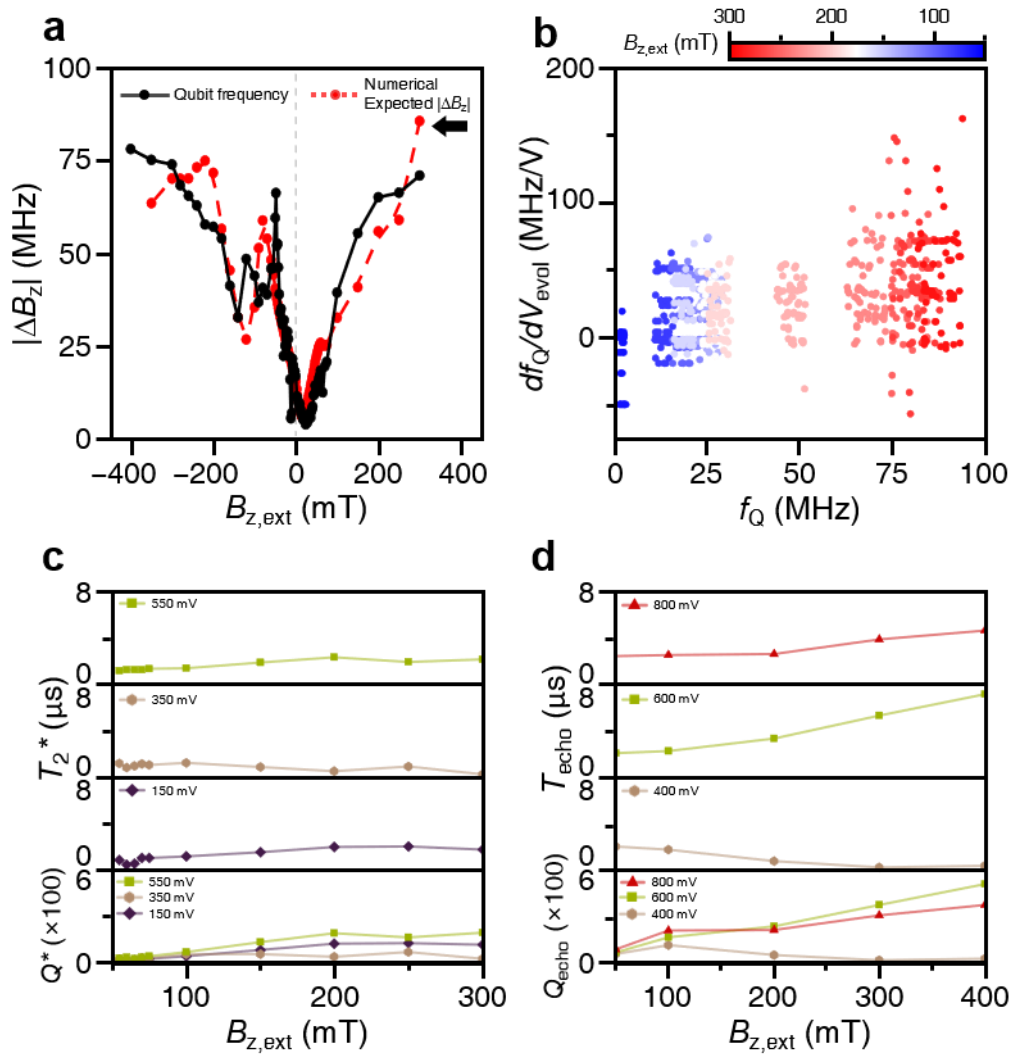


Fig. 4 | External magnetic field dependence of coherence time. (a) Estimated $|\Delta B_z|$ extracted from f_Q of the Ramsey oscillation performed for $V_{\text{evol}} = 800$ mV in the ΔB_z -dominating region (black), and expected $|\Delta B_z|$ from the magnetic field simulation using OOMMF (red) (see Supplementary Information S5). The black arrow indicates the direction of the measurement. (b) Extracted f_Q and charge susceptibility df_Q/dV_{evol} of the qubit in $B_{z,\text{ext}}$ of 300–40 mT and V_{evol} of 0.4–0.7 V. df_Q/dV_{evol} was derived with interpolated f_Q . (c) Measured T_2^* , Q^* of the Ramsey oscillations as a function of $B_{z,\text{ext}}$ at various V_{evol} . (d) T_{echo} and Q_{echo} , the results of the spin-echo experiment of T_2^* and Q^* , respectively, as a function of $B_{z,\text{ext}}$ at various V_{evol} .

Figure 5.

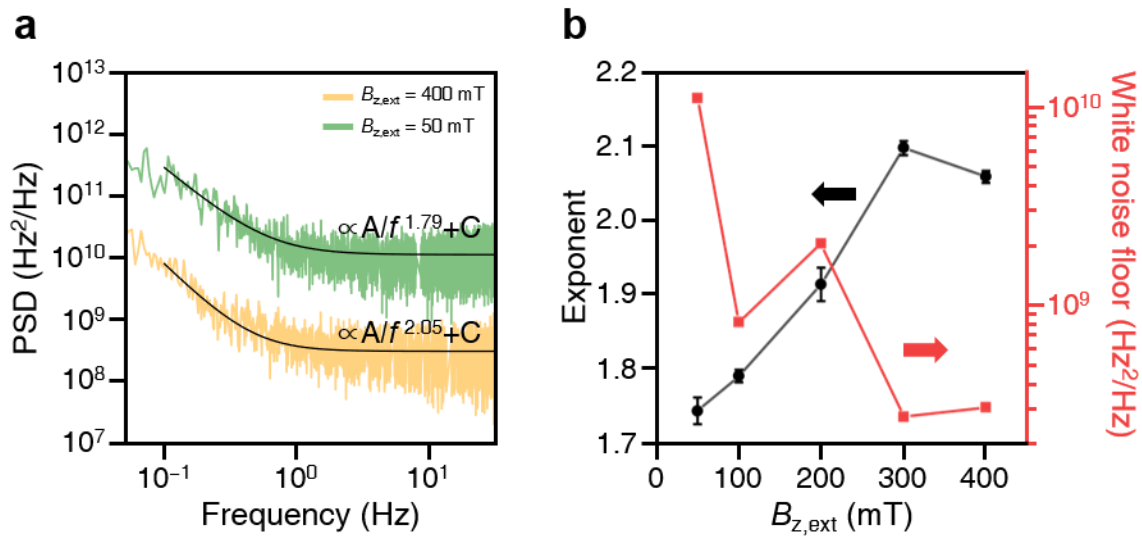


Fig. 5 | Noise spectrum analysis. (a) Noise spectrum acquired by applying two different $B_{z,\text{ext}}$. Power spectral densities (PSDs) were derived by analyzing single-shot data with the rapid Bayesian estimation method (see Supplementary Information S7). Each noise spectrum was calculated using 100,000 single shots. Offsets were excluded from this figure. (b) Power-law exponent and white noise floor level obtained from the noise spectrum at each $B_{z,\text{ext}}$.

References

1. Loss, D. & DiVincenzo, D. P. Quantum computation with quantum dots. *Phys. Rev. A* **57**, 120–126 (1998).
2. Petta, J. R. *et al.* Coherent Manipulation of Coupled Electron Spins in Semiconductor Quantum Dots. *Science* **309**, 2180–2184 (2005).
3. Koppens, F. H. L. *et al.* Driven coherent oscillations of a single electron spin in a quantum dot. *Nature* **442**, 766–771 (2006).
4. Nadj-Perge, S., Frolov, S. M., Bakkers, E. P. A. M. & Kouwenhoven, L. P. Spin–orbit qubit in a semiconductor nanowire. *Nature* **468**, 1084–1087 (2010).
5. Van Den Berg, J. W. G. *et al.* Fast Spin-Orbit Qubit in an Indium Antimonide Nanowire. *Phys. Rev. Lett.* **110**, 066806 (2013).
6. Pioro-Ladrière, M. *et al.* Electrically driven single-electron spin resonance in a slanting Zeeman field. *Nature Physics* **4**, 776–779 (2008).
7. Takeda, K. *et al.* A fault-tolerant addressable spin qubit in a natural silicon quantum dot. *Science advances* **2**, e1600694 (2016).
8. Scappucci, G. *et al.* The germanium quantum information route. *Nature Review Materials* **6**, 926–943 (2020).
9. Maurand, R. *et al.* A CMOS silicon spin qubit. *Nature Communications* **7**, 13575 (2016).
10. Jock, R. M. *et al.* A silicon metal-oxide-semiconductor electron spin-orbit qubit. *Nature Communications* **9**, 1768 (2018).
11. Maune, B. M. *et al.* Coherent singlet-triplet oscillations in a silicon-based double quantum dot. *Nature* **481**, 344–347 (2012).
12. Kawakami, E. *et al.* Electrical control of a long-lived spin qubit in a Si/SiGe quantum dot. *Nature Nanotechnology* **9**, 666–670 (2014).
13. Yoneda, J. *et al.* A quantum-dot spin qubit with coherence limited by charge noise and

- fidelity higher than 99.9%. *Nature Nanotechnology* **13**, 102–106 (2018).
14. Wu, X. *et al.* Two-axis control of a singlet–triplet qubit with an integrated micromagnet. *Proceedings of the National Academy of Sciences* **111**, 11938–11942 (2014).
 15. Takeda, K., Noiri, A., Yoneda, J., Nakajima, T. & Tarucha, S. Resonantly Driven Singlet-Triplet Spin Qubit in Silicon. *Phys. Rev. Lett.* **124**, 117701 (2020).
 16. Jock, R. M. *et al.* A silicon singlet–triplet qubit driven by spin-valley coupling. *Nature Communications* **13**, 641 (2022).
 17. Cai, X., Connors, E. J., Edge, L. F. & Nichol, J. M. Coherent spin–valley oscillations in silicon. *Nature Physics* **19**, 386–393 (2023).
 18. Dumoulin Stuyck, N. I. *et al.* Low dephasing and robust micromagnet designs for silicon spin qubits. *Applied Physics Letters* **119**, (2021).
 19. Reilly, D. J., Marcus, C. M., Hanson, M. P. & Gossard, A. C. Fast single-charge sensing with a rf quantum point contact. *Applied Physics Letters* **91**, 162101 (2007).
 20. Noiri, A. *et al.* Radio-Frequency-Detected Fast Charge Sensing in Undoped Silicon Quantum Dots. *Nano Letters* **20**, 947–952 (2020).
 21. Ono, K., Austing, D. G., Tokura, Y. & Tarucha, S. Current Rectification by Pauli Exclusion in a Weakly Coupled Double Quantum Dot System. *Science* **297**, 1313–1317 (2002).
 22. Orona, L. A. *et al.* Readout of singlet-triplet qubits at large magnetic field gradients. *Phys. Rev. B* **98**, 125404 (2018).
 23. Harvey-Collard, P. *et al.* High-Fidelity Single-Shot Readout for a Spin Qubit via an Enhanced Latching Mechanism. *Phys. Rev. X* **8**, 021046 (2018).
 24. Nakajima, T. *et al.* Robust Single-Shot Spin Measurement with 99.5% Fidelity in a Quantum Dot Array. *Phys. Rev. Lett.* **119**, 017701 (2017).
 25. Fogarty, M. A. *et al.* Integrated silicon qubit platform with single-spin addressability,

- exchange control and single-shot singlet-triplet readout. *Nature Communications* **9**, 4370 (2018).
26. Delbecq, M. R. *et al.* Quantum Dephasing in a Gated GaAs Triple Quantum Dot due to Nonergodic Noise. *Phys. Rev. Lett.* **116**, 046802 (2016).
 27. Connors, E. J., Nelson, J., Qiao, H., Edge, L. F. & Nichol, J. M. Low-frequency charge noise in Si/SiGe quantum dots. *Phys. Rev. B* **100**, (2019).
 28. Struck, T. *et al.* Low-frequency spin qubit energy splitting noise in highly purified ²⁸Si/SiGe. *npj Quantum Information* **6**, 40 (2020).
 29. Shi, Z. *et al.* Tunable singlet-triplet splitting in a few-electron Si/SiGe quantum dot. *Applied Physics Letters* **99**, 233108 (2011).
 30. Breuer, H.-P. & Petruccione, F. *The theory of open quantum systems*. (Clarendon, 2007).
 31. Donahue, M. J. & Porter, D. G. OOMMF User's Guide, Version 1.0. (1999).
 32. Neumann, R. & Schreiber, L. R. Simulation of micro-magnet stray-field dynamics for spin qubit manipulation. *Journal of Applied Physics* **117**, 193903 (2015).
 33. Connors, E. J., Nelson, J., Edge, L. F. & Nichol, J. M. Charge-noise spectroscopy of Si/SiGe quantum dots via dynamically-decoupled exchange oscillations. *Nature Communications* **13**, 940 (2022).
 34. Zhao, R. *et al.* Single-spin qubits in isotopically enriched silicon at low magnetic field. *Nature Communications* **10**, 5500 (2019).
 35. Sergeevich, A., Chandran, A., Combes, J., Bartlett, S. D. & Wiseman, H. M. Characterization of a qubit Hamiltonian using adaptive measurements in a fixed basis. *Phys. Rev. A* **84**, 052315 (2011).
 36. Shulman, M. D. *et al.* Suppressing qubit dephasing using real-time Hamiltonian estimation. *Nature Communications* **5**, 5156 (2014).

37. Nagaraja, H. S. *et al.* Magnetic Domain Studies of Cobalt Nanostructures. *J Supercond Nov Magn* **25**, 1901–1906 (2012).
38. Mi, X., Cady, J. V., Zajac, D. M., Deelman, P. W. & Petta, J. R. Strong coupling of a single electron in silicon to a microwave photon. *Science* **355**, 156–158 (2017).
39. Mi, X. *et al.* A coherent spin–photon interface in silicon. *Nature* **555**, 599–603 (2018).
40. Veldhorst, M. *et al.* An addressable quantum dot qubit with fault-tolerant control-fidelity. *Nature Nanotechnology* **9**, 981–985 (2014).

Supplementary Information

Supplementary Note 1. Signal-to-noise ratio (SNR) of the charge sensor

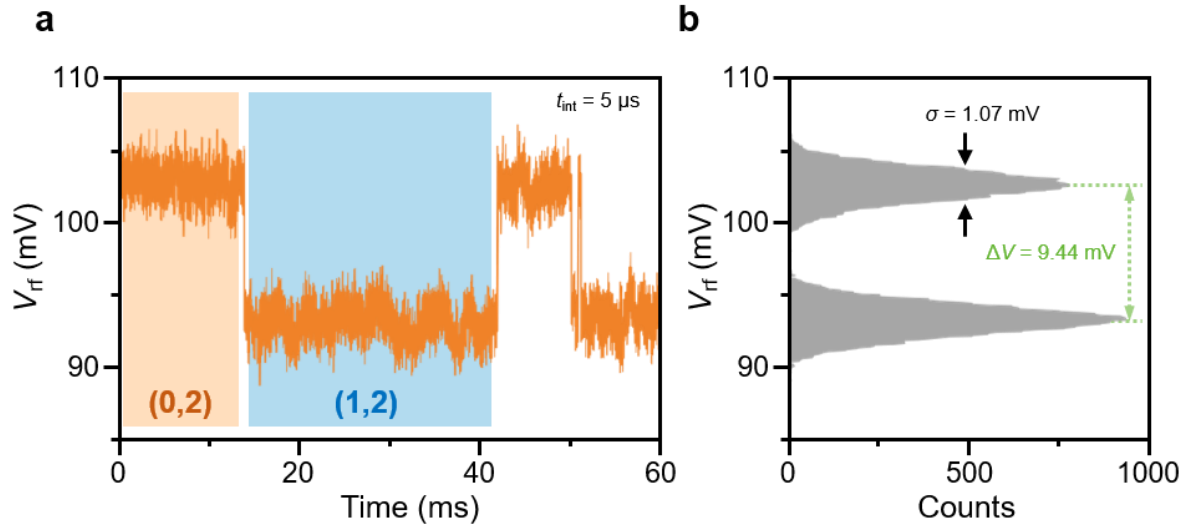


Fig. S1 | Single electron charge transition signal. (a) Demodulated sensor signal (V_{rf}) during single electron charge transitions from the left dot with integration time $t_{int} = 5 \mu\text{s}$, and (b) its histogram. The SNR is defined by $\Delta V/\sigma$, where ΔV is the signal contrast of V_{rf} for a single electron charge transition and σ is the root-mean-square noise amplitude at a given t_{int} . ΔV and σ are estimated to be 9.44 mV and 1.07 mV, respectively, yielding the SNR to be 8.82. This SNR alone would limit the state measurement infidelity $< 1\%$, thus we regard the observed quantum oscillation visibility about 85% in the main text is limited by additional measurement error such as the triplet state relaxation during the readout and imperfect singlet state initialization after measurement.

Supplementary Note 2. DC tuning dependency of the kink in the Ramsey interferometry

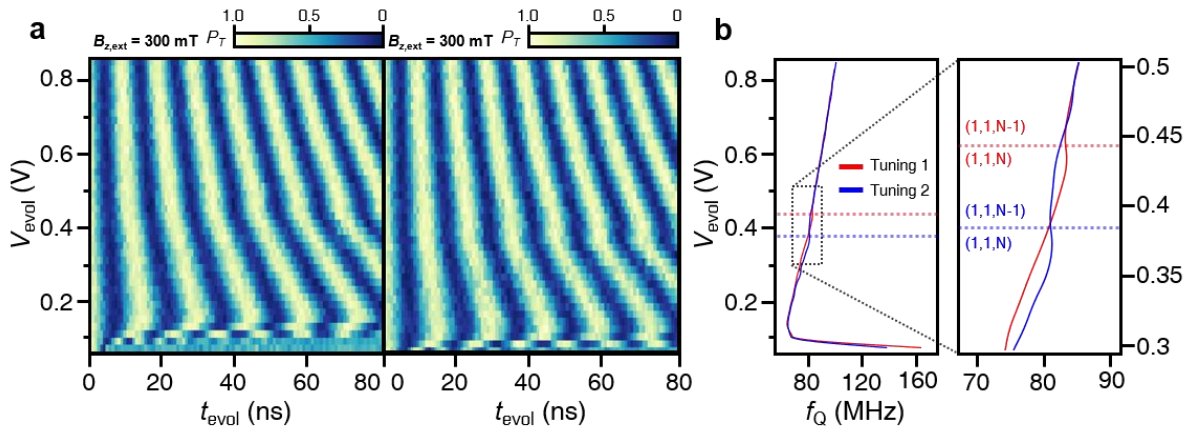


Fig. S2 | Tunable kink in the Ramsey interferometry depending on the tuning condition. (a) The Ramsey interferometry result under the DC voltage tuning condition same as in Fig. 2c of the main text (left panel, tuning 1) and with an additional -40 mV gate voltage applied to the plunger gate of QD_R (right panel, tuning 2). The nearby gate voltages were appropriately tuned to enable state preparation and readout. (b) The interpolated line-to-line FFT result of (a), showing the systematic change of the kink point. The horizontal dotted lines indicate the kink point and the numbers in parenthesis represent the number of electrons of QD_L , QD_M , and QD_R , while both are shown with the red (blue) color for the data extracted under the tuning 1 (tuning 2) condition. The result indicates that the abrupt frequency shift in the Ramsey interferometry is correlated with the ground state charge transition in QD_R .

Supplementary Note 3. Disappearance of the coherent coupling in weak magnetic fields

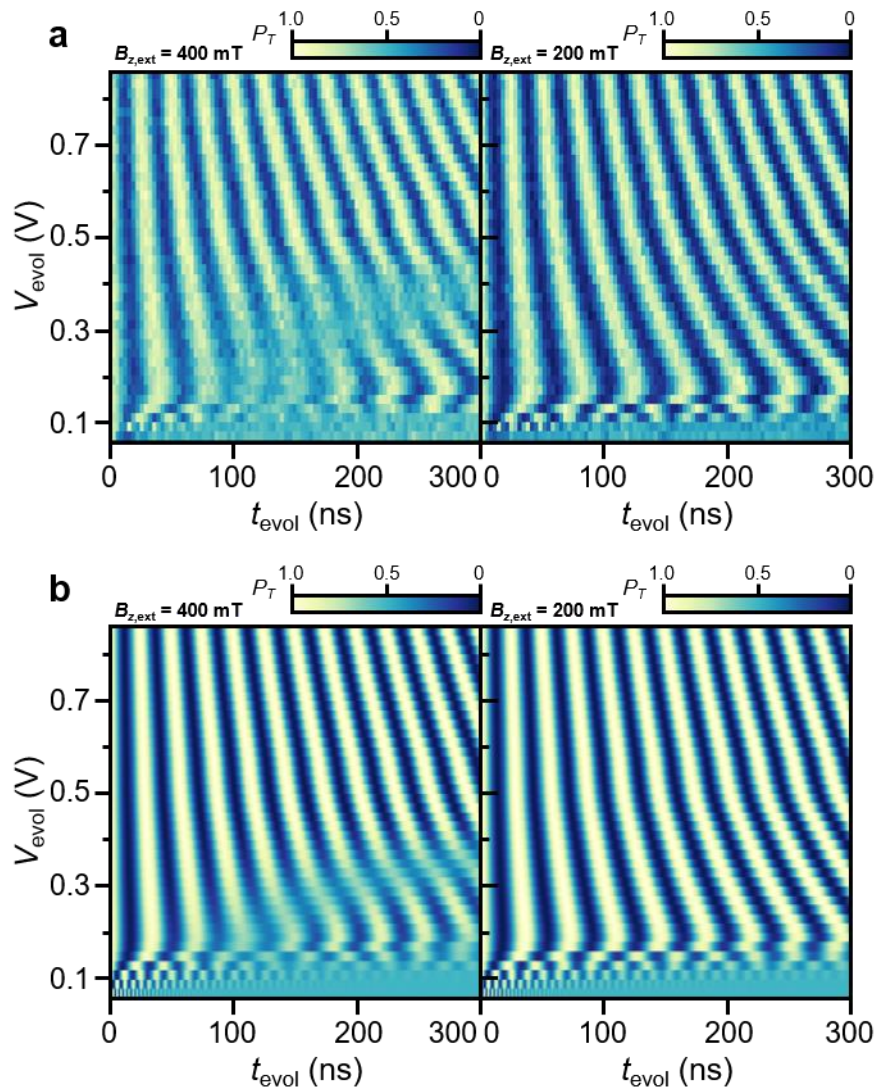


Fig. S3 | Exchange spectroscopy in two different magnetic fields. (a) The exchange spectroscopy result obtained using the pulse sequence depicted in Fig. 2a of the main text at two different magnetic fields (left: $B_{z,\text{ext}} = 400$ mT, right: $B_{z,\text{ext}} = 200$ mT). Note that the beating of the oscillation disappears as the magnetic field decreases, indicating that the eigenstate of the many-electron qubit depends on the magnetic field. (b) The simulation results obtained by solving the Lindblad master equation using the Hamiltonian described in Eqn. S1. The simulation results consistently reproduce the disappearance of the beating when the magnetic field is decreased from 400 mT to 200 mT, in support of the interpretation of the Zeeman-split spin levels in QD_R as described in the main text.

Supplementary Note 4. Details of the numerical simulation of the Ramsey interferometry

In the main text, we implemented the Hamiltonian of the two interacting qubits to simulate the exchange spectroscopy result of the ST_0 qubit. Specifically, the Hamiltonian of the many-electron qubit (QD_R) that couples with ST_0 qubit is assumed to have a diagonal term with exponential detuning dependence and an off-diagonal term with linear magnetic field dependence. The coupling between the qubits is assumed to have the form of $J_{\text{int}}(V_{\text{evol}})\sigma_x \otimes \sigma_z$, and the coupling strength $J_{\text{int}}(V_{\text{evol}})$ is chosen to be the linear function of the detuning based on the spectroscopy result of Fig 3a of the main text. In addition, to incorporate the change in the charge state of the nearby N-electron quantum dot, the coupling term is multiplied by a phenomenological Fermi-Dirac distribution. Labeling ST_0 and QD_R subspace with the subscript of S and R, the Hamiltonian in the Hilbert space $\mathcal{H}_S \otimes \mathcal{H}_R$ is expressed as below:

$$H(V_{\text{evol}}, B_{z,\text{ext}}) = J(V_{\text{evol}})\sigma_z \otimes \mathbf{1} + \Delta B_z(V_{\text{evol}}, B_{z,\text{ext}})\sigma_x \otimes \mathbf{1} + \beta(V_{\text{evol}})\mathbf{1} \otimes \sigma_z + \gamma(B_{z,\text{ext}})\mathbf{1} \otimes \sigma_x + J_{\text{int}}(V_{\text{evol}}) \frac{1}{e^{\eta(\beta(V_{\text{evol}}-c))}} \sigma_x \otimes \sigma_z \quad (\text{S1})$$

, where $\mathbf{1}$ is a 2-dimensional identity matrix, $\beta(V_{\text{evol}}) = A_1 + A_2 \exp((A_3 - V_{\text{evol}})/\alpha)$ is the exponential function of detuning, and $\gamma(B_{z,\text{ext}}) = \kappa(B_{z,\text{ext}} - \delta)\theta(B_{z,\text{ext}} - \delta)$ is the linear function κ of the magnetic field multiplied by the Heaviside step function θ for computational efficiency. Proper constants c , η , $A_{i=1,2,3}$, α and δ were used for enhancing the accuracy of numerical simulation.

Our specific choice for the form of the QD_R Hamiltonian is primarily informed by the observations presented in Fig. S3a, where the beating of the oscillation of the ST_0 qubit disappears at certain $B_{z,\text{ext}}$ and V_{evol} values. As these observations reveal the dependence on $B_{z,\text{ext}}$ and V_{evol} of the eigenaxis of QD_R , we introduced the diagonal term $\beta(V_{\text{evol}})$ and the off-

diagonal term $\gamma(B_{z,\text{ext}})$. To elucidate further, the off-diagonal term $\gamma(B_{z,\text{ext}})$ ensures a nonnegligible $\gamma(B_{z,\text{ext}})$ value when $B_{z,\text{ext}}$ reaches a sufficiently large magnitude. Concurrently, the diagonal term $\beta(V_{\text{evol}})$ imparts the exponential dependence on V_{evol} to the eigenaxis of QD_R. Therefore, when $B_{z,\text{ext}}$ is large enough such that $\gamma(B_{z,\text{ext}})$ is nonnegligible, the eigenstates of the QD_R align closely with the σ_x -eigenstates below a certain V_{evol} threshold. In contrast, when $B_{z,\text{ext}}$ is small enough to the extent that $\gamma(B_{z,\text{ext}})$ is negligible, the eigenstates of the QD_R remain the σ_z -eigenstates regardless of V_{evol} values of interest. Since the σ_x -eigenstates are the superposition of the σ_z -eigenstates whose orbital wavefunction directly couples with the qubit frequency of ST₀ qubits, this gives rise to the beating of the oscillation at certain V_{evol} and $B_{z,\text{ext}}$ values.

The simulation results of the exchange spectroscopy in the main text and supplementary information are obtained with the single qubit dephasing Lindbladian of $\tau_1\sqrt{J(V_{\text{evol}})}\sigma_z \otimes \mathbf{1}$ and $\tau_2\sqrt{\beta(V_{\text{evol}})}\mathbf{1} \otimes \sigma_z$ with dephasing rates $\gamma_S = J(V_{\text{evol}})\tau_1^2$ and $\gamma_M = \beta(V_{\text{evol}})\tau_2^2$. Here, assuming that the voltage fluctuation induces the dephasing of each qubit, we set γ_S and γ_M to be proportional to $J(V_{\text{evol}})$ and $\beta(V_{\text{evol}})$, respectively. In addition, throughout the simulation, the proportionality constants for ST₀ qubit and $J_{\text{int}}(V_{\text{evol}})$, which are accessible from the experimental results, were determined by fitting the formula to the experimental data. On the contrary, the inaccessible proportionality functions and constants for QD_R, such as κ and α , were selected to give the results that fit the experimental data well. The exchange spectroscopy was simulated by numerically solving the Quantum Master equation (QME) in a Lindblad form, with $V_{\text{evol}}(t)$ of the pulse sequence depicted in Fig. 2a of the main text.

Supplementary Note 5. Numerical micromagnetic simulation

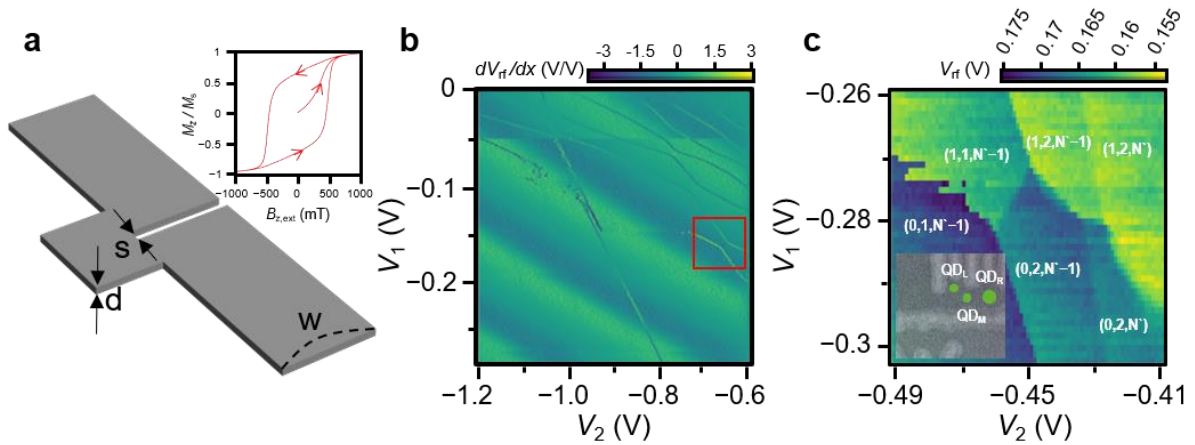


Fig. S4 | On-chip Co Micromagnet. (a) The design of the micromagnet used in our study. For simulation, we set the parameters with thickness $d = 128$ nm, width $w = 2.112$ μm and gap $s = 288$ nm. Inset: The hysteresis curve with magnetization in z -direction M_z/M_s , with $B_{z,ext}$ swept between ± 2000 mT and -2000 mT starting at 0 mT. (b) Charge stability diagram while the plunger gate and right barrier gate of QD_R are fully merged with the right reservoir, indicating that QD_L and QD_M for the ST_0 qubit reside inside the region formed by the three left most surface gates. The red box indicates the primary operational region. (c) Charge stability diagram after forming the third, many-electron quantum dot QD_R .

We used Object Oriented Micromagnetic Framework (OOMMF) to calculate numerically expected $|\Delta B_z|$, which solves Landau-Lifshitz-Gilbert equation¹ for each time step to obtain the magnetization in each mesh with a given magnetic field. We modeled the 3-dimensional shape of the micromagnet (Fig. S4a) we used in this study, consisting of polycrystalline cobalt². The magnetization process was done by driving $B_{z,ext}$ parameter back and forth from 500 mT to -500 mT several times, similar to the magnetization process we adopted. The following parameters were used in the simulations: Uniaxial anisotropy constant $K_1 = 7.5 \times 10^5$ J/m³, $K_2 = 1.5 \times 10^5$ J/m, exchange constant $A = 2.906 \times 10^{11}$ J/m, saturation magnetization $M_s = 1.467 \times 10^6$ A/m, Landau-Lifshitz gyromagnetic ratio $\gamma_{LL} = 2.409 \times 10^5$ m/(As), Gilbert damping parameter 0.5, and the cubic mesh size = 32 nm. Some of the parameters were referred from the previous study³ which analyzed this micromagnet design with numerical simulation earlier, and we could reproduced similar hysteresis loop (see inset of Fig. S4a) with aforementioned study using those parameters.

For calculating numerically expected $|\Delta B_z|$, we used Gaussian averaged B_z , with diameter at 25nm and its center at the expected position of QD_L and QD_M. To explore the expected position of QD_L and QD_M, we formed the quantum dot using only the three left most gates and backbone gates (see Fig. S4b). The charge stability diagram indicates that QD_L and QD_M are likely located inside the region formed by the three left most gates. Subsequent formation of QD_R and its coupling with the ST₀ qubit is shown in Fig. S5c. We selected the expected position of each of two quantum dots (see inset of Fig. S4c) where the numerically expected $|\Delta B_z|$ results most fit the measured $|\Delta B_z|$ result, and this dot position also showed consistency from the actual experiment, which we revealed from Fig. S4b and Fig. S4c. The numerically expected distance between QD_L and QD_M was ~ 100 nm. The vertical distance between the bottom of the magnet and the quantum dots for simulation was 163nm, estimated from the device structure.

Supplementary Note 6. Effect of total data acquisition time on the coherence time

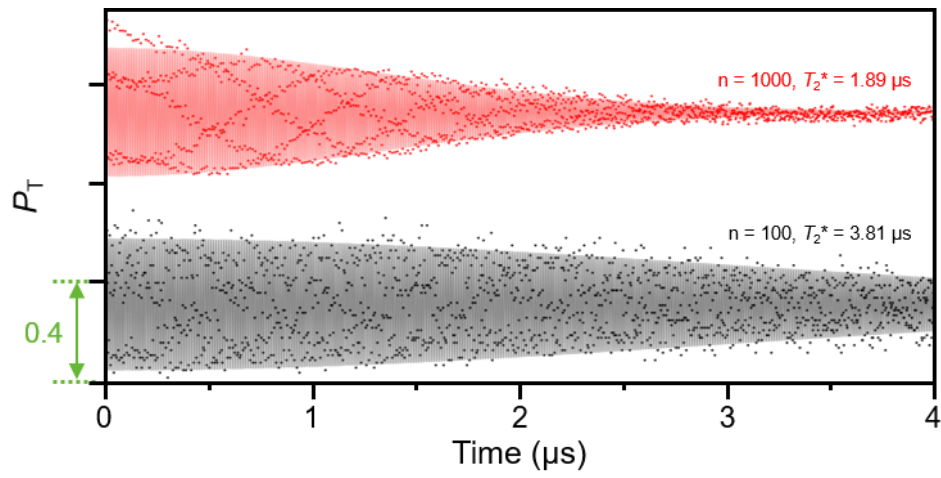


Fig. S5 | Ramsey oscillation with different data acquisition times. The magnetic field driven qubit oscillation traces of ST_0 qubit at $B_{z,\text{ext}} = 400$ mT with the number of single-shot experiments for each data point $n = 100$ (lower trace) and $n = 1000$ (upper trace). The traces are offset by 0.7 for clarity. Even at relatively strong $B_{z,\text{ext}} = 400$ mT, increasing total data acquisition time leads to reduced the coherence time indicating the significant portion of low frequency noise in the system.

Supplementary Note 7. Bayesian frequency estimation and power spectral density

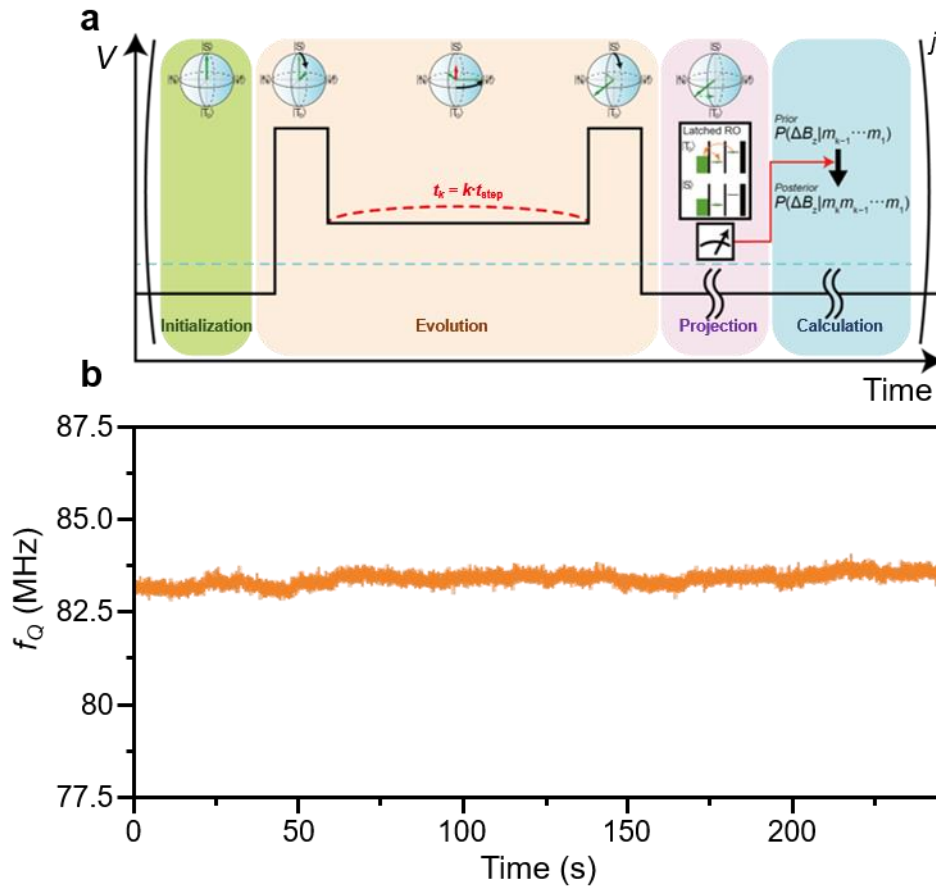


Fig. S6 | Bayesian estimation for ST_0 qubit. (a) Schematic of Bayesian estimation circuit for ST_0 qubit, used in our study. (b) Example of the time trace of f_Q using the circuit (a) at $B_{z,\text{ext}} = 400$ mT.

The Bayesian estimation circuit, illustrated in Fig. S6a, starts with the initialization step, where we first initialize ST_0 qubit to the singlet state. This step is followed by the evolution step, where we manipulate the qubit at a specific detuning for free evolution V_{evol} with a given evolution time t_k that linearly increase in step of t_{step} up to a given number of maximum iteration j . The subsequent projective single-shot measurement of ST_0 qubit is performed by the latched readout method described in the main text. Based on the single-shot measurement result, Bayesian inference of the qubit frequency f_Q is performed by the following rule up to a normalization constant:

$$P(f_Q | m_j, m_{j-1}, \dots, m_1) = P_0(f_Q) \prod_{k=1}^j \frac{1}{2} \{1 + r_k [\alpha + \beta \cos(2\pi f_Q t_k)]\}$$

, where $r_k = 1(-1)$ for $m_k = |S\rangle(|T_0\rangle)$, and $\alpha(\beta)$ is the parameter determined by the axis of rotation (oscillation visibility). Starting from the prior uniform initial distribution $P_0(f_Q)$, the narrow posterior distribution $P(f_Q | m_j, m_{j-1}, \dots, m_1)$ is obtained after j^{th} Bayesian estimation and f_Q is estimated where the probability value is the maximum. In our study, we set $\alpha = -0.05$, $\beta = 0.6$, $t_{\text{step}} = 1.6$ ns and $j = 200$ for Bayesian estimation. The time trace of f_Q (see Fig. S6b, as an example) is converted to power spectral density in the frequency domain by fast Fourier transform and the Welch's method⁴ was used for smoothing the spectrum.

Supplementary References

1. Gilbert, T. L. Classics in Magnetism A Phenomenological Theory of Damping in Ferromagnetic Materials. *IEEE Trans. Magn.* **40**, 3443–3449 (2004).
2. Nagaraja, H. S. *et al.* Magnetic Domain Studies of Cobalt Nanostructures. *J Supercond Nov Magn* **25**, 1901–1906 (2012).
3. Neumann, R. & Schreiber, L. R. Simulation of micro-magnet stray-field dynamics for spin qubit manipulation. *Journal of Applied Physics* **117**, 193903 (2015).
4. Welch, P. The use of fast Fourier transform for the estimation of power spectra: A method based on time averaging over short, modified periodograms. *IEEE Trans. Audio Electroacoust.* **15**, 70–73 (1967).